Inorganic Chemistry

Article

pubs.acs.org/IC

Novel Soft-Chemistry Route of $Ag_2Mo_3O_{10}{\cdot}2H_2O$ Nanowires and in Situ Photogeneration of a $Ag@Ag_2Mo_3O_{10}{\cdot}2H_2O$ Plasmonic Heterostructure

Khadija Hakouk,[†] Philippe Deniard,[†] Luc Lajaunie,[†] Catherine Guillot-Deudon,[†] Sylvie Harel,[†] Zeyan Wang,[∥] Baibiao Huang,[∥] Hyun-Joo Koo,[‡] Myung-Hwan Whangbo,[§] Stéphane Jobic,[†] and Rémi Dessapt*,[†]

[†]Institut des Matériaux Jean Rouxel, Université de Nantes, CNRS, 2 rue de la Houssinière, BP 32229, 44322 Nantes Cedex, France
[‡]Department of Chemistry and Research Institute for Basic Sciences, Kyung Hee University, Seoul 130-701, Republic of Korea
[§]Department of Chemistry, North Carolina State University, Raleigh, North Carolina 27695-8204, United States
[∥]State Key Lab of Crystal Materials, Shandong University, Jinan 250100, China

S *Supporting Information*

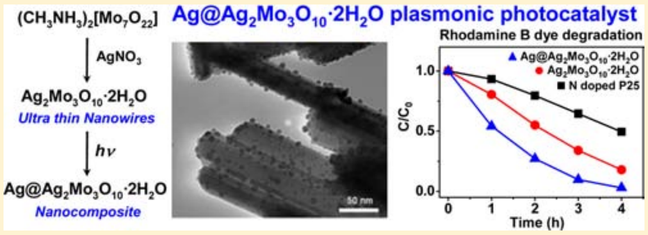

ABSTRACT: Ultrathin $Ag_2Mo_3O_{10}{\cdot}2H_2O$ nanowires (NWs) were synthesized by soft chemistry under atmospheric pressure from a hybrid organic−inorganic polyoxometalate $(CH_3NH_3)_2[Mo_7O_{22}]$ and characterized by powder X-ray diffraction, DSC/TGA analyses, FT-IR and FT-Raman spectroscopies, scanning electron microscopy (SEM), and transmission electron microscopy (TEM). Their diameters are a few tens of nanometers and hence much thinner than that found for silver molybdates commonly obtained under hydrothermal conditions. The optical properties of $Ag_2Mo_3O_{10}{\cdot}2H_2O$ NWs before and after UV irradiation were investigated by UV−vis−NIR diffuse reflectance spectroscopy revealing, in addition to photoreduction of Mo^{6+} to Mo^{5+} cations, in situ photogeneration of well-dispersed silver Ag^0 nanoparticles on the surface of the NWs. The resulting $Ag@Ag_2Mo_3O_{10}{\cdot}2H_2O$ heterostructure was confirmed by electron energy-loss spectroscopy (EELS), X-ray photoelectron spectroscopy (XPS), and Auger spectroscopy. Concomitant reduction of Mo^{6+} and Ag^+ cations under UV excitation was discussed on the basis of electronic band structure calculations. The $Ag@Ag_2Mo_3O_{10}{\cdot}2H_2O$ nanocomposite is an efficient visible-light-driven plasmonic photocatalyst for degradation of Rhodamine B dye in aqueous solution.

1. INTRODUCTION

Plasmonic photocatalysts[1] are a promising class of materials that exploits the unique optical properties of noble metal nanoparticles (NPs) combined with semiconductors to generate efficient photocatalytic reactions active for visible-light water splitting,[2] pollutant destruction,[3] and bacterial disinfection.[4] Noble metal NPs exhibit strong absorption in the visible region due to localized surface plasmon resonance (LSPR) produced by the collective oscillations of the electrons on the surface of the NPs.[5] For a given surrounding medium, this resonance wavelength can be fine tuned by varying the size and shape of the NPs and, to a lesser extent, their concentration.[6] This has allowed one to generate a wide range of noble metal NPs@semiconductor nanocomposites with very interesting photocatalytic performances, although the exact role of metal particles is still open to debate. To date, enhancement of the photocatalytic performances of semiconductors in contact with NPs is commonly attributed to the more efficient charge carrier segregation (formation of Schottky barrier, for instance) and a strong absorption of the impinging light.[1b]

Recently, studies have shown that Ag@AgX (X = Cl, Br) heterostructures[7] are excellent and stable visible-light-driven plasmonic photocatalysts for dye decomposition. The Ag NPs absorb visible light, prevent photogenerated electrons from combining with Ag^+ cations, and allow formation of activated X^0 atoms by combining X^- ions with photogenerated holes. As expected, the morphology of the Ag@AgX microstructures as well as the nature of the X^- ion strongly influences the photocatalytic performance.[8,9] Plasmonic photocatalysts based on Ag^0 or Au^0 NPs supported on the surface of metal−oxide semiconductors have also been extensively investigated.[1b,10] For example, TiO_2 is a widely used, nontoxic, and inexpensive photocatalyst[11] but is not effective under visible light due to its large band gap (e.g., 3.2 eV for anatase). Ag−TiO_2 nanocomposites[12] have been successfully developed which allow extending the outstanding performance of TiO_2 under UV toward the visible region and improving electron−hole pair segregation. Currently, the most frequently used synthesis

Received: February 8, 2013
Published: May 16, 2013

ACS Publications dx.doi.org/10.1021/ic400343v | *Inorg. Chem.* 2013, 52, 6440−6449

strategy to obtain such Ag@metal−oxide semiconductor heterostructures is the photodeposition method which consists of immersing the metal−oxide in a solution containing silver cations and exposing the mixture to high-power UV irradiation.[1b,10d,13] Reduction of Ag^+ cations into Ag^0 NPs is thus induced by the photogenerated electron−hole pairs into the semiconductor, associated with oxidation of the solvent molecules. A shortcoming of this approach is poor control over the NPs size distribution and their inhomogeneous deposition onto the semiconductor surface. Thus, it is desirable to develop a simple and an efficient alternative route to reach Ag@metal−oxide semiconductor nanocomposites which avoids implication of a solid−liquid interface. We thus expected that crystallized hydrated silver metalates or polyoxometalates (POM) might be used as efficient precursors in an all solid state photodeposition method. Silver polyoxomolybdates appear as promising candidates to confirm this expectation. For instance, Feng et al. have recently reported a hydrothermal based synthesis of $Ag_2Mo_3O_{10}\cdot 1.8H_2O$ nanowires (NWs) with an average diameter of 80−200 nm.[14] Under high power-light irradiation (300 W Xe lamp), Ag^0 NPs were photogenerated at the surface of the NWs and the resulting heterostructure shows significant photocatalytic activity for degradation of Rhodamine B (RhB) dye solution under visible-light irradiation. Nevertheless, the in situ formation mechanism of the photoinduced silver@silver molybdate nanocomposite is to date unknown and deserves to be investigated. In addition, since the dye photodegradation processes take place on the surface of the NWs, their surface area should drastically influence the efficiency of the photocatalytic reactions considering that the smaller the thickness of the NWs the higher the photocatalytic performance of the photocatalyst. Consequently, developing new strategies to reach finer hydrated silver molybdate NWs is an exciting challenge.

In this work, we reported a new efficient route to synthesize, under ambient pressure, pure and very thin $Ag_2Mo_3O_{10}\cdot 2H_2O$ NWs (average diameter in the range 20−50 nm) with a high surface area, starting from a hybrid organic−inorganic material based on layered POM units and organoammonium cations (OAC) (see section 2). The optical properties of the $Ag_2Mo_3O_{10}\cdot 2H_2O$ NWs, before and after UV irradiation at 254 nm, have been investigated by diffuse reflectance spectroscopy in section 3, and they have been compared with those of $(H_2DABCO)[Mo_3O_{10}]\cdot H_2O$,[15] i.e., an OAC/POM reference containing the same $^{1}/_{\infty}[Mo_3O_{10}]^{2-}$ unit.[16] Optical measurements have revealed that both Ag^+ and Mo^{6+} cations are photoreduced into the $Ag_2Mo_3O_{10}\cdot 2H_2O$ NWs under low-power UV exposure. Section 4 describes the characterization of the photogenerated Ag^0 NPs on the surface of the $Ag_2Mo_3O_{10}\cdot 2H_2O$ NWs by transmission electron microscopy (TEM) analysis, X-ray photoelectron spectroscopy (XPS), Auger spectroscopy, and electron energy-loss spectroscopy (EELS). A possible formation mechanism for the resulting $Ag@Ag_2Mo_3O_{10}\cdot 2H_2O$ heterostructure has been proposed in section 5, which involves photoreduction of both the Ag^+ and the Mo^{6+} cations. The photocatalytic activities of $Ag_2Mo_3O_{10}\cdot 2H_2O$ NWs and $Ag@Ag_2Mo_3O_{10}\cdot 2H_2O$ under visible light have been investigated in section 6. The essential findings of this work are summarized in section 7.

2. SYNTHESIS AND STRUCTURE CHARACTERIZATION OF $Ag_2Mo_3O_{10}\cdot 2H_2O$ NWS

$Ag_2Mo_3O_{10}\cdot 2H_2O$ NWs were successfully synthesized via the unprecedented two-step soft-chemistry route displayed in Scheme 1. First, the hybrid organic−inorganic layered OAC/POM compound $(CH_3NH_3)_2[Mo_7O_{22}]$ was quantitatively obtained by acidifying at pH 1 a mother solution initially containing $Na_2MoO_4\cdot 2H_2O$ and an excess of $CH_3NH_3^+$ cations and after keeping the mixture under mild hydrothermal conditions at 120 °C for 6 h. Second, the as-prepared $(CH_3NH_3)_2[Mo_7O_{22}]$ reacted with a stoichiometric amount of $AgNO_3$ in 0.1 M HNO_3 at 80 °C and under atmospheric pressure for 3 h to quantitatively precipitate $Ag_2Mo_3O_{10}\cdot 2H_2O$ as a pale yellow fibrillar powder (see Experimental Section for details).

Scheme 1. New Two-Step Soft-Chemistry Route of $Ag_2Mo_3O_{10}\cdot 2H_2O$ Nanowires (NWs)

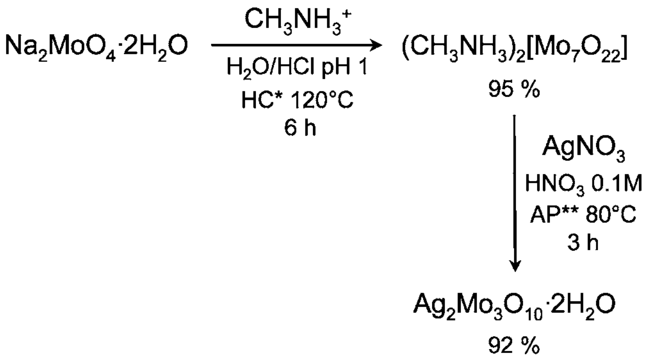

*HC = Hydrothermal Conditions
**AP = Ambient Pressure

The structure of $Ag_2Mo_3O_{10}\cdot 2H_2O$ was refined with the Rietveld[17] profile refinement technique by means of the JANA 2006 program[18] starting from the structural model of Wlodarczyk-Gajda et al.[19] Background was modeled with a Legendre polynomial. Bragg peak profile instrument contribution was taken into account using the fundamental approach,[20,21] namely, thanks to a complete description of both the diffractometer optics and the energy distribution of the X-ray tube, the instrument resolution is fully calculated. Hence, the compound contribution (crystallite size and eventually microstrain) can be obtained directly from deconvolution as refinable parameters. In good agreement with a nanowire-like shape of the material (see below), an anisotropic crystal size was determined to be ~50.0(3) and ~30.0(5) nm along and perpendicular to the running axis of the crystallites, respectively. Despite careful preparation of the sample, a slight preferred orientation could not be avoided and was refined using the March-Dollase[22] function (po = 0.905(2)). The final reliability factors under the *Pnma* space group (a = 13.2182(3) Å, b = 7.5968(2) Å, c = 9.7610(2) Å) are R_{wp} = 7.52%, R_p = 5.75%, Gof = 1.93%, and R_B = 2.66%. The final residual electron density obtained from difference Fourier calculation is $-0.91\ e^-/Å^3 < \rho < +0.87\ e^-/Å^3$. It is worth noting that the final positions of some oxygen atoms deviate as far as 0.5 Å from Wlodarczyk-Gajda et al.'s structural model. Figure 1 shows the quality of the refinement. Some residues appear on the difference curve, but these discrepancies are not related to troubles in the structure determination since they also exist in the Le Bail refinement procedure. Probably

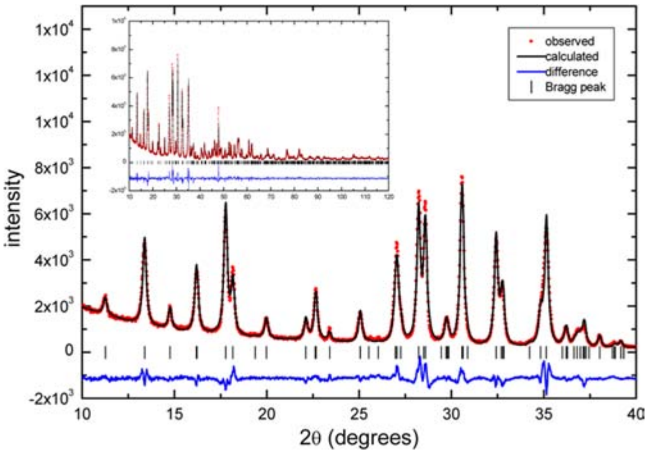

Figure 1. XRD observed, calculated, and difference patterns of $Ag_2Mo_3O_{10}·2H_2O$ after Rietveld refinement.

they are the signature of a more complex particle size anisotropy since no contribution of microstrains to the peak shape profile is observed. All atom positions are gathered in Table S1, Supporting Information. Obviously, the hydrogen atoms of the water molecules were not introduced in the Rietveld procedure. Nevertheless, from bond valence calculations[23] they are found to be linked to O8 (to form the hereafter labeled H$_2$O_2 molecule) and O9 (to form the hereafter labeled H$_2$O_1 molecule) that evidence valence sums of 0.18 and 0.35, respectively, in the hydrogen-free model.

The structure of $Ag_2Mo_3O_{10}·2H_2O$ is depicted in Figure 2. This compound contains the polymeric $^1/_\infty[Mo_3O_{10}]^{2-}$ POM unit (Figure 2a). This zigzag infinite chain is built upon trimeric $\{Mo_3O_{13}\}$ subunits composed of three distorted edge-shared $[MoO_6]$ octahedra. The $^1/_\infty[Mo_3O_{10}]^{2-}$ blocks run along the *b* axis (Figure 2b) and are associated in the framework with two crystallographically independent Ag$^+$ cations (hereafter labeled Ag1 and Ag2) in distorted octahedral environments and two crystallized water molecules. Ag1 connects two $^1/_\infty[Mo_3O_{10}]^{2-}$ chains and two water molecules (H$_2$O_1), while Ag2 connects three $^1/_\infty[Mo_3O_{10}]^{2-}$ chains and one water molecule (H$_2$O_2). Very, interestingly, H$_2$O_1 and H$_2$O_2 also connect the $^1/_\infty[Mo_3O_{10}]^{2-}$ units via one and two H bonds, respectively (Figure 2c). This strongly impacts the thermal behavior of the material. Formally, the TGA and DSC curves of $Ag_2Mo_3O_{10}·2H_2O$ show two distinct weight losses of 2.80% and 2.53% in the ranges of 25−110 and 110−265 °C, respectively, which correspond to endothermic effects (see Figure S1, Supporting Information). Both weight losses can be attributed to removal of one type of water molecules (theoretical weight loss of 2.6% per water molecule). Moreover, the weight losses occur in very distinct temperature ranges, showing clearly that one water molecule is more strongly linked to the network than the other (see section 5).

The SEM and TEM images of $Ag_2Mo_3O_{10}·2H_2O$ (Figure 3) show uniform NWs that have diameters ranging from 20 to 50 nm and lengths up to several hundred micrometers. According to the crystal structure described above, this suggests that NWs are built upon elongated crystallites staked along the *b* axis. It is worth noting that the average diameter of the NWs is much smaller than that of silver molybdate NWs obtained from other synthesis routes using hydrothermal treatments.[14,24] This leads to a large specific surface area (22.0 m^2/g) for $Ag_2Mo_3O_{10}·2H_2O$ NWs compared with those reported for other silver molybdate photocatalysts.[25] The results clearly emphasize the efficiency of this new synthesis route to generate very thin $Ag_2Mo_3O_{10}·2H_2O$ NWs, namely, the as-described synthesis of $Ag_2Mo_3O_{10}·2H_2O$ NWs occurs according to eq 1.

$$3(CH_3NH_3)_2[Mo_7O_{22}] + 14Ag^+ + 18H_2O \rightarrow 7Ag_2Mo_3O_{10}·2H_2O + 8H^+ + 6CH_3NH_3^+ \quad (1)$$

It implies conversion in solution of the $^2/_\infty[Mo_7O_{22}]^{2-}$ unit into the less acidic $^1/_\infty[Mo_3O_{10}]^{2-}$ one, inducing a noticeable decrease in the pH of the solution. Then, the trimolybdate

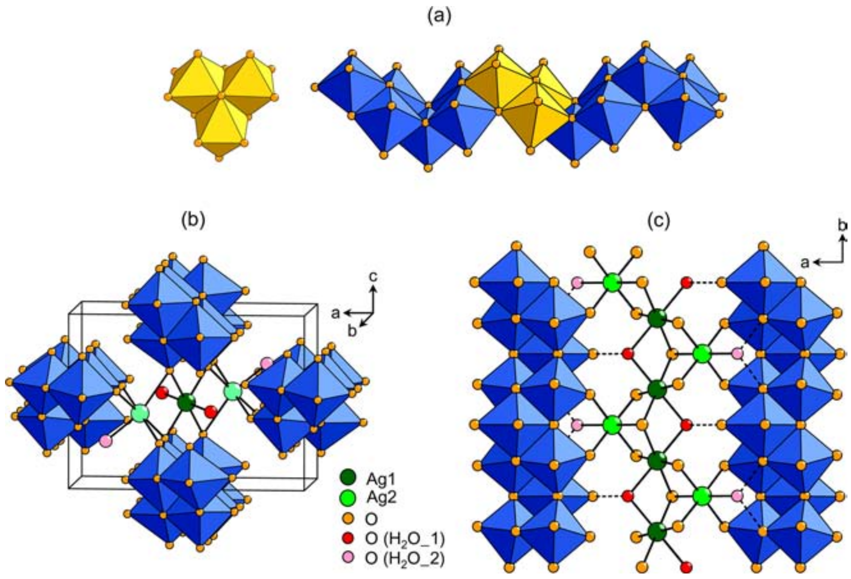

Figure 2. (a) Representations of the $\{Mo_3O_{13}\}$ trimer (in yellow) and polymeric $^1/_\infty[Mo_3O_{10}]^{2-}$ block in $Ag_2Mo_3O_{10}·2H_2O$ built upon the $\{Mo_3O_{13}\}$ subunits edge-shared condensed in a zigzag chain. (b) Representation of the distinct distorted octahedral environments of the two crystallographically independent silver cations in $Ag_2Mo_3O_{10}·2H_2O$. (c) Representation of the different H-bonding subnetworks between the two crystallized water molecules and the $^1/_\infty[Mo_3O_{10}]^{2-}$ units in $Ag_2Mo_3O_{10}·2H_2O$.

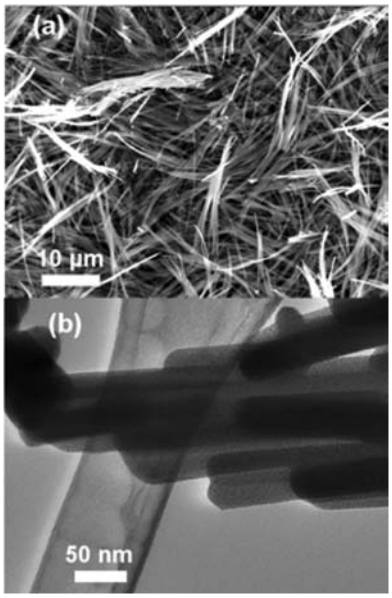

Figure 3. (a) SEM image of thin $Ag_2Mo_3O_{10}·2H_2O$ nanowires (NWs) synthesized in ambient pressure at 80 °C from $(CH_3NH_3)_2[Mo_7O_{22}]$. (b) TEM micrographs of $Ag_2Mo_3O_{10}·2H_2O$ NWs with an average diameter of 20−50 nm.

entity rapidly precipitates with Ag^+ cations. At first sight, due to its very low solubility in acidic solution under ambient pressure, degradation of $(CH_3NH_3)_2[Mo_7O_{22}]$ may release Mo^{6+} cations to the solution very slowly, which promotes growth of finer silver trimolybdate NWs than does the use of hydrothermal routes.

3. OPTICAL CHARACTERIZATION

As shown in Figure 4a, $Ag_2Mo_3O_{10}·2H_2O$ and $(H_2DABCO)[Mo_3O_{10}]·H_2O$—a $^1/_\infty[Mo_3O_{10}]^{2-}$ containing OAC/POM reference—have an absorption threshold of 3.0 and 3.7 eV, respectively. The energy of the optical gap of $(H_2DABCO)[Mo_3O_{10}]·H_2O$ which results in strong $O^{2-} \rightarrow Mo^{6+}$ ligand-to-metal charge transfer into the $^1/_\infty[Mo_3O_{10}]^{2-}$ unit is similar to that of other OAC/POM systems built upon the same trimolybdate block.[26] In the case of $Ag_2Mo_3O_{10}·2H_2O$ NWs, the optical gap is drastically reduced to 3.0 eV. This can be explained by considering that the silver cations contribute to the valence band (VB) through strong hybridization between O 2p and Ag 4d orbitals,[27] with the Ag 4d orbitals lying above the O 2p orbitals (Figure 4b) (see section 5 for details).

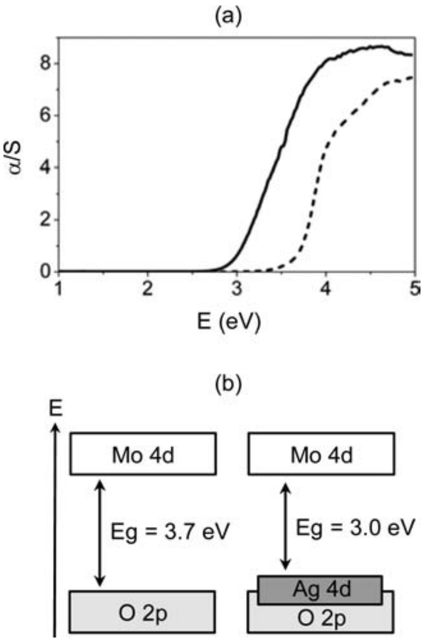

Figure 4. (a) Kubelka−Munk transformed reflectivity vs energy of $(H_2DABCO)[Mo_3O_{10}]·H_2O$ (---) and $Ag_2Mo_3O_{10}·2H_2O$ (——). (b) Schematic representations of the band structures and optical band gaps of $(H_2DABCO)[Mo_3O_{10}]·H_2O$ (left) and $Ag_2Mo_3O_{10}·2H_2O$ (right).

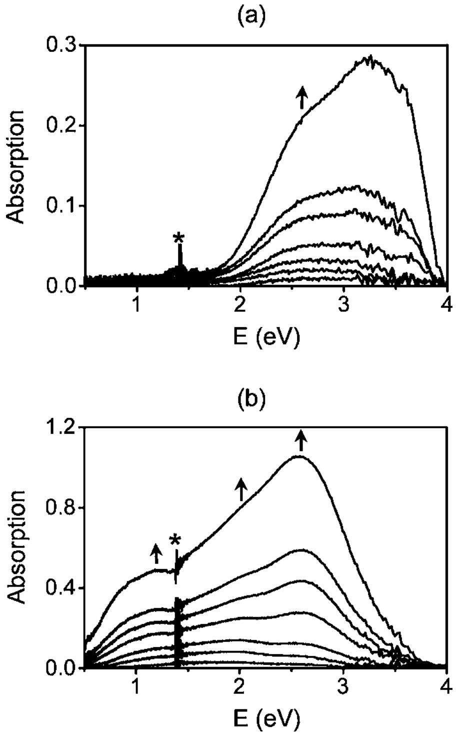

Figure 5. Evolution of photogenerated absorption versus irradiation time *t* of (a) $(H_2DABCO)[Mo_3O_{10}]·H_2O$ and (b) $Ag_2Mo_3O_{10}·2H_2O$ after 1, 5, 10, 20, 30, 40, and 80 min of UV irradiation at 254 nm. Positions in energy of the photogenerated absorption bands are indicated by arrows. Asterisk denotes the position in energy of an artifact due to the change in detector.

Under UV excitation (254 nm, 6 W), the color of the powder of $(H_2DABCO)[Mo_3O_{10}]·H_2O$ gradually shifts from white to brown with increasing irradiation time. As illustrated in Figure 5a, the color change is associated with growth of a broad absorption band in the visible located at 2.60 eV (477 nm). The coloration is then due to the UV-induced reduction of Mo^{6+} to Mo^{5+} cations according to the well-established mechanism in photochromic OAC/POM systems.[28] By comparison, evolution of the photogenerated absorption of $Ag_2Mo_3O_{10}·2H_2O$ NWs under similar UV exposure is given in Figure 5b. As observed for $(H_2DABCO)[Mo_3O_{10}]·H_2O$, a broad absorption band around 2.60 eV (477 nm) grows up with irradiation time. In parallel, other less intense broad absorption bands show up around 1.15 (1078 nm) and 2.00 eV (620 nm), and the color of the sample gradually shifts from pale yellow to dark gray. By analogy with $(H_2DABCO)[Mo_3O_{10}]·H_2O$, the absorption at 2.60 eV in the spectra of UV-irradiated $Ag_2Mo_3O_{10}·2H_2O$ NWs can be attributed to the presence of photoreduced Mo^{5+} cations into the $^1/_\infty[Mo_3O_{10}]^{2-}$ block. Assignment of the other absorption bands could be ascribed to the LSPR of silver metal NPs photogenerated from $Ag_2Mo_3O_{10}·2H_2O$ NWs and well characterized from the TEM, EELS, and Auger experiments (see section 4). This assignment is in good accordance with the recent work of Feng et al.[14] and the fact that Ag^0 LSPR, often reported at about 410 nm in the literature,[29] can be red shifted due to changes in the particle morphology and the surrounding medium. Let us notice that the possibility of silver NPs contributing also to the absorption peak at 2.60 eV cannot be fully excluded.

4. CHARACTERIZATION OF THE PHOTOINDUCED $Ag@Ag_2Mo_3O_{10}·2H_2O$ NANOSTRUCTURE

Figure 6a shows a TEM micrograph collected at liquid nitrogen temperature of $Ag_2Mo_3O_{10}·2H_2O$ initially irradiated at 254 nm for 4 h. Quasi-spherical NPs randomly decorate the surface of the NWs, and most of them have an average diameter around 10 nm. EELS analyses were performed on these NPs and areas in their direct vicinity to gain information on their chemical composition. EELS spectra of both the NWs and the deposited NPs are displayed in Figure 6b together with the reported Ag^0 bulk spectra as reference.[30] Only the Mo-$M_{2,3}$ (around 400 eV) and O-K (around 530 eV) edges are observed for the NWs nearby the NPs and only the Ag-$M_{4,5}$ edge (around 400 eV) for the NPs. Furthermore, the energy-loss fine structures of the NPs match perfectly those of Ag^0 bulk, although comparison of spectra recorded under different experimental conditions requires special attention. Consequently, EELS experiments evidence photogeneration of Ag^0 NPs on the backbone of the NWs under UV excitation, with depletion of silver element in the immediate vicinity of the NPs.

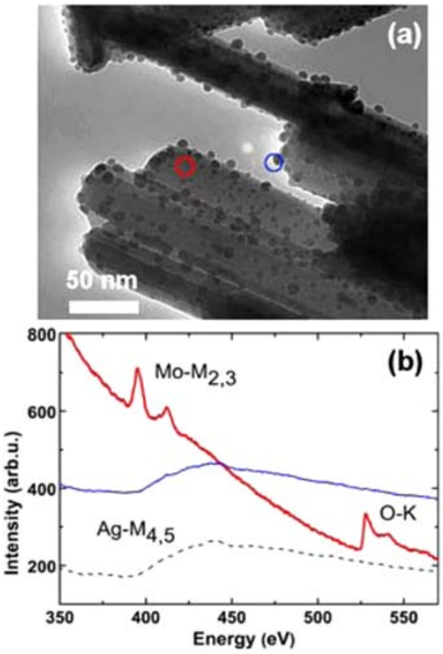

Figure 6. (a) TEM micrographs of $Ag_2Mo_3O_{10}·2H_2O$ NWs after 254 nm UV irradiation for 4 h. Probed areas studied by EELS are highlighted by red and blue circles for the nanowire and nanoparticle, respectively. (b) EELS spectra ranging from 350 to 570 eV for the nanowire (thick red line), nanoparticle (thin blue line), and bulk Ag (dotted line, taken from ref 30).

To confirm these results, XPS and Auger analyses were carried out on $Ag_2Mo_3O_{10}·2H_2O$ pellets before and after 254 nm UV irradiation for 4 h. Binding energies of the Mo $3d_{5/2}$ and $3d_{3/2}$ lines for the nonirradiated $Ag_2Mo_3O_{10}·2H_2O$ NWs are located at 232.5 and 235.6 eV, respectively, in agreement with that reported, for example, for pure α-MoO_3 that also contains Mo^{6+} cations in distorted octahedral environments.[31] After UV irradiation, the Mo $3d_{5/2}$ and $3d_{3/2}$ peaks do not show significant changes, except for a low spreading, which can be attributed to partial reduction of Mo^{6+} ions into Mo^{5+} ones (see Figure S2, Supporting Information). Ag 3d XPS spectra of $Ag_2Mo_3O_{10}·2H_2O$ before and after exposure to UV light are displayed Figure 7a. The intensity of the Ag $3d_{5/2}$ peak drastically increases after irradiation, indicating a more important quantity of Ag element at the surface of the NWs. The Ag $3d_{5/2}$ shape and binding energy (~367.9 eV) after UV irradiation remain quite unchanged. This binding energy is in good agreement with those already reported for the Ag^+ state,[32] but it is well known that identification of the chemical states is not straightforward in the case of the Ag element because the Ag 3d shift between the Ag metal and the Ag^+ cation in silver oxides is in the range of a few tenths of an eV (maximum 0.4 eV). Thus, in the case of $Ag_2Mo_3O_{10}·2H_2O$ NWs covered by Ag^0 NPs, the Ag chemical states are difficult to discern from Ag 3d XPS spectra only.[32a]

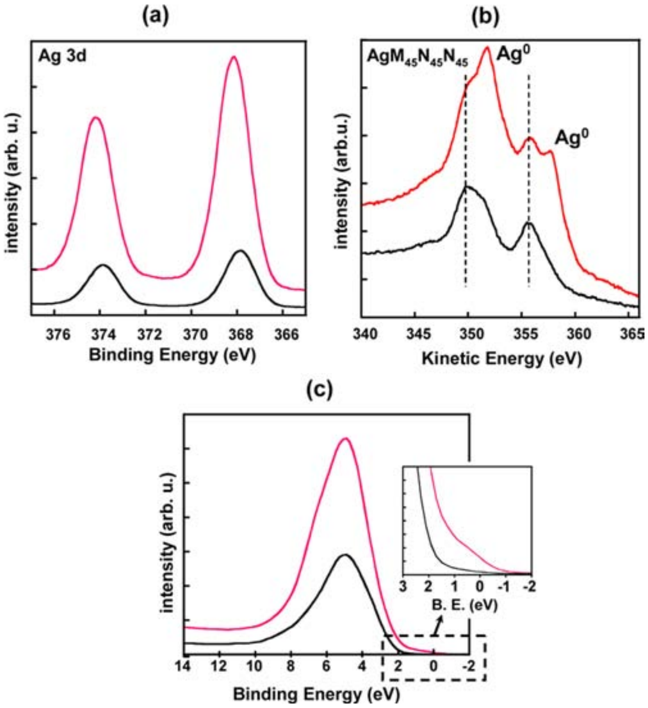

Figure 7. (a) XPS Ag3d spectra, (b) MNN Auger electron spectra, and (c) valence band structures of $Ag_2Mo_3O_{10}·2H_2O$ NWs obtained before (black) and after (red) 254 nm UV irradiation for 4 h.

By contrast, examination of Auger spectra is often useful for identifying chemical states since Auger peaks are usually more sensitive to chemical environments than photoelectron peaks. Auger Ag spectra of $Ag_2Mo_3O_{10}·2H_2O$ before and after UV irradiation are displayed in Figure 7b. Before irradiation, the Ag MNN Auger shape agrees with that of the Ag^+ cation in silver oxides with two peaks ($M_5N_{4,5}N_{4,5}$ and $M_4N_{4,5}N_{4,5}$) located around 350 and 356 eV, respectively. These values are comparable to those reported for Ag_2O.[32b,c] After UV exposure, two more intense supplementary peaks appear at higher kinetic energies (352 and 357.5 eV) and are assigned to metallic silver.[32c,33] This latter observation is confirmed by studying the valence band of $Ag_2Mo_3O_{10}\cdot 2H_2O$ before and after UV irradiation (Figure 7c). Before UV irradiation, the valence band is made up of a unique broad band in the 2−10 eV energy range with a maximum located at around 5 eV. The maximum position corresponds quite nicely to Ag 4d states,[32b] in agreement with DFT calculations (see below), and no metallic states at the Fermi level E_F are apparent in this case. After irradiation, the valence band exhibits a drastic increase in intensity without changing the shape and peak position. In addition, metallic states are clearly detected at E_F. This low-intensity metallic feature is close to that observed at E_F for silver metal.[34] Thus, the valence band spectra strengthen the conclusion that Ag^+ cations are photoreduced in the material and the resulting Ag^0 atoms aggregate into NPs. The latter grow under UV irradiation and migrate to the surface of the $Ag_2Mo_3O_{10}\cdot 2H_2O$ NWs to create the $Ag@Ag_2Mo_3O_{10}\cdot 2H_2O$ nanostructure, as observed by TEM and EELS analyses.

5. ELECTRONIC STRUCTURE OF $Ag_2Mo_3O_{10}\cdot 2H_2O$ AND POSSIBLE UV-INDUCED FORMATION MECHANISM OF THE $Ag@Ag_2Mo_3O_{10}\cdot 2H_2O$ NANOSTRUCTURE

The projected density of states (PDOS) plots calculated for the optimized structure of $Ag_2Mo_3O_{10}\cdot 2H_2O$ are displayed in Figure S3, Supporting Information, with the zero energy level chosen at the Fermi level. As expected, the 4d bands of the Mo atoms are located above E_F and constitute the major contribution of the conduction band. The 4d-block bands of Ag1 and Ag2 lie at the top of the valence band with a higher contribution of the Ag1 orbitals to the uppermost levels, namely, the 4d bands located around E_F are mainly made up of antibonding combinations between Ag 4d and O 2p. Those antibonding levels move to a higher energy region with increasing strength of the orbital interactions between the Ag and the O atoms. Thus, the Ag1 atoms interact more strongly with the surrounding O atoms than do the Ag2 atoms. Below −7.5 eV, the O 2p peak of H_2O_1 (with O9) lies slightly lower in energy than that of H_2O_2 (with O8), thereby implying that H_2O_1 is more strongly attached to Ag1 than is H_2O_2 to Ag2. Thus, removal of H_2O_2 might be easier than that of H_2O_1 from $Ag_2Mo_3O_{10}\cdot 2H_2O$ as the temperature is raised. To confirm this implication, we evaluate the relative energies for the optimized structure of $Ag_2Mo_3O_{10}\cdot H_2O$ obtained by removing either H_2O_1 or H_2O_2. In good agreement with this suggestion, our calculations show that $Ag_2Mo_3O_{10}\cdot H_2O$ obtained by removing H_2O_2 is more stable than that obtained by removing H_2O_1 (by 5.1 kcal/mol per formula unit), i.e., weight losses at 110 and 265 °C on the TGA curve (Figure S1 in the Supporting Information) are associated with departure of H_2O_2 and H_2O_1 molecules, respectively.

Let us now consider a possible formation mechanism of the $Ag@Ag_2Mo_3O_{10}\cdot 2H_2O$ nanostructure which involves both reduction of Mo^{6+} and Ag^+ cations into Mo^{5+} cations and Ag^0 NPs, respectively, when the $Ag_2Mo_3O_{10}\cdot 2H_2O$ NWs are exposed under UV excitation (or under irradiation with an energy near its optical band gap). According to the coloration mechanism of photochromic OAC/POM systems,[28] photoreduction of Mo^{6+} into Mo^{5+} ions requires the presence of labile H atoms which move from the OACs onto the POM units to create hydroxyl groups in the vicinity of the reducible Mo^{6+} cations. A similar photoinduced hydrogen displacement is currently admitted to describe the photochromic behavior of MoO_3 under UV excitation, and the observed color change is assigned to insertion of protons from protic molecules physisorbed on the oxide surface.[35] In the case of $Ag_2Mo_3O_{10}\cdot 2H_2O$ NWs, photoreduction of Mo^{6+} and Ag^+ cations might be associated with oxidation of the crystallized water molecules (oxidation of a trace of physisorbed water molecules can be neglected because, according to TGA analyses, its amount is insignificant compared with that of the crystallized water molecules). Comparison of the near-infrared spectra of $Ag_2Mo_3O_{10}\cdot 2H_2O$ NWs before and after 254 nm UV irradiation for 4 h reveals the loss of crystallized water molecules in the irradiated sample (Figure S4, Supporting Information). Considering both the crystal and the electronic structures of $Ag_2Mo_3O_{10}\cdot 2H_2O$ and according to all characterizations described above, the formation mechanism of the $Ag@Ag_2Mo_3O_{10}\cdot 2H_2O$ nanostructure might involve the following steps.

(a) Irradiation of $Ag_2Mo_3O_{10}\cdot 2H_2O$ NWs transfers an electron from the top of the valence band into the conduction one. Thus, the electron/hole pair segregation leads to formation of Mo^{5+} and unstable high-oxidizing Ag^{2+} cations[36] in the material, as indicated in eq 2.

$$Mo^{6+} + Ag^{+} + h\nu \rightarrow Mo^{5+} + Ag^{2+} \tag{2}$$

(b) The crystallized water molecules H_2O_1 and H_2O_2 directly connected to the photogenerated Ag^{2+} cations may be oxidized, generating Ag^0 atoms, which could aggregate to form the Ag^0 NPs, and releasing protons, in agreement with eqs 3 and 4.

$$H_2O \rightarrow 1/2O_2 + 2H^{+} + 2e^{-} \tag{3}$$

$$Ag^{2+} + 2e^{-} \rightarrow Ag^{0} \tag{4}$$

(c) As both H_2O_1 and H_2O_2 also connect the ${}^{1}/_{\infty}[Mo_3O_{10}]^{2-}$ units, protons might be transferred onto adjacent $[MoO_6]$ octahedra to stabilize photoreduced Mo^{5+} cations, according to eq 5.

$$2[Mo^{5+}O_6] + 2H^{+} \rightarrow 2[Mo^{5+}O_5OH] \tag{5}$$

Growth of Ag^0 NPs at the surface of the $Ag_2Mo_3O_{10}\cdot 2H_2O$ NWs induces local destruction of the hydrated silver trimolybdate network and formation of a new phase, which remains undetected so far (neither by powder X-ray diffraction techniques nor by IR and Raman spectroscopies), and is expected to be a member of the H_xMoO_3 series.

6. PHOTOCATALYTIC PROPERTIES

In order to evaluate the photocatalytic performances of as-prepared yellow pale $Ag_2Mo_3O_{10}\cdot 2H_2O$ NWs and dark gray $Ag@Ag_2Mo_3O_{10}\cdot 2H_2O$ NWs, obtained by initially irradiated $Ag_2Mo_3O_{10}\cdot 2H_2O$ NWs under UV (254 nm) for 6 h, photocatalytic bleaching of Rhodamine B dye (RhB) aqueous solutions was carried out under visible-light irradiation ($\lambda > 420$ nm). For comparison, N-doped P25 powders, prepared by direct nitridation of commercially available P25 powders under NH_3 atmosphere (hereafter noted as N-P25), were used as a standard visible-light reference. Figure 8 shows the C/C_0 vs t plots for three samples (C_0 and C refer to concentrations of the

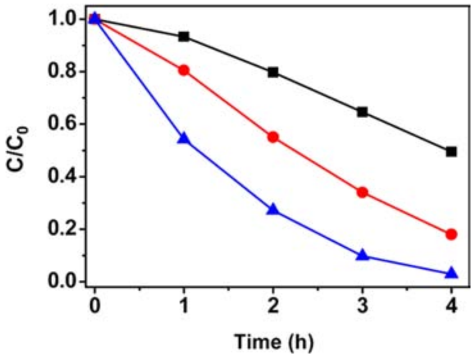

Figure 8. C/C_0 vs t plots for photo-oxidation of RhB under visible light (λ > 420 nm) in the presence of N-P25 (■), as-prepared $Ag_2Mo_3O_{10}\cdot 2H_2O$ NWs (●), and $Ag@Ag_2Mo_3O_{10}\cdot 2H_2O$ nanocomposite (▲).

RhB dye before irradiation and at irradiation time t, respectively). About 80% of RhB is decomposed after irradiation under visible light for 4 h in the presence of the $Ag_2Mo_3O_{10}\cdot 2H_2O$ NWs but only 50% of RhB in the presence of N-P25. Under the same conditions, about 97% of RhB is decomposed using $Ag@Ag_2Mo_3O_{10}\cdot 2H_2O$ NWs. This clearly indicates that both $Ag_2Mo_3O_{10}\cdot 2H_2O$ and $Ag@Ag_2Mo_3O_{10}\cdot 2H_2O$ NWs exhibit higher photocatalytic activities than does N-P25 under visible-light irradiation, and photocatalytic decomposition of RhB over the $Ag@Ag_2Mo_3O_{10}\cdot 2H_2O$ NWs is faster than that of the as-prepared $Ag_2Mo_3O_{10}\cdot 2H_2O$ NWs.

The corresponding time-dependent absorption spectra of the RhB solution in the presence of the three photocatalysts are displayed in Figure 9. In each case, the maximum absorption band of the RhB aqueous solution (centered at 553 nm) decreases, in agreement with photodegradation of the dye under visible-light irradiation. Absorptions were continuously blue shifted with time for $Ag_2Mo_3O_{10}\cdot 2H_2O$ and $Ag@Ag_2Mo_3O_{10}\cdot 2H_2O$ NWs contrary to the case of N-P25. This indicates that the RhB molecules were de-ethylated in a stepwise manner, and the ethyl groups are removed one by one once they are in contact with the silver trimolybdate NWs during photocatalytic experiments.[37] Formally, the new absorption at 500 nm can be attributed to formation of fully de-ethylated RhB molecules.[38] The improved performance of $Ag@Ag_2Mo_3O_{10}\cdot 2H_2O$ NWs compared with that of $Ag_2Mo_3O_{10}\cdot 2H_2O$ NWs is related to preliminary photogeneration of Ag^0 NPs and Mo^{5+} centers, which yield enhanced visible-light absorptions. Moreover, the existence of Ag^0 NPs could also promote the efficiency of the photoinduced charge separation/transfer and lead to higher photocatalytic activities. Thus, it is suggested that the $Ag@Ag_2Mo_3O_{10}\cdot 2H_2O$ NWs could be used as an efficient visible-light photocatalyst.

7. CONCLUDING REMARKS

Very thin $Ag_2Mo_3O_{10}\cdot 2H_2O$ NWs with a high specific surface area were successfully prepared via a new soft-chemistry route in aqueous solution and under ambient pressure. The $Ag@Ag_2Mo_3O_{10}\cdot 2H_2O$ nanocomposite can be easily in situ obtained by exposing the photosensitive $Ag_2Mo_3O_{10}\cdot 2H_2O$ NWs under a low-power UV irradiation. These results show that hydrated silver metalates or polyoxometalates are efficient precursors in an alternative "all solid state" photodeposition method for easily reaching Ag@metal—oxide semiconductor heterostructures. In addition, we evidenced that Mo^{5+} cations are also photogenerated in $Ag_2Mo_3O_{10}\cdot 2H_2O$ NWs. At first sight, reduction of both Ag^+ and Mo^{6+} ions is associated with oxidation of the crystallized water molecules which link the metal cations in the framework and formation of the $Ag@Ag_2Mo_3O_{10}\cdot 2H_2O$ nanocomposite might involve photogeneration of Ag^{2+} cations as high-oxidizing intermediary species. $Ag@Ag_2Mo_3O_{10}\cdot 2H_2O$ NWs are an efficient visible-light plasmonic photocatalyst to degradation of the RhB dye. We are now working to extend this synthesis strategy to other hydrated silver polyoxometalates and consolidate the proposed formation mechanism. Notably, the influence of the nature of the POM block on the photocatalytic performance is under study.

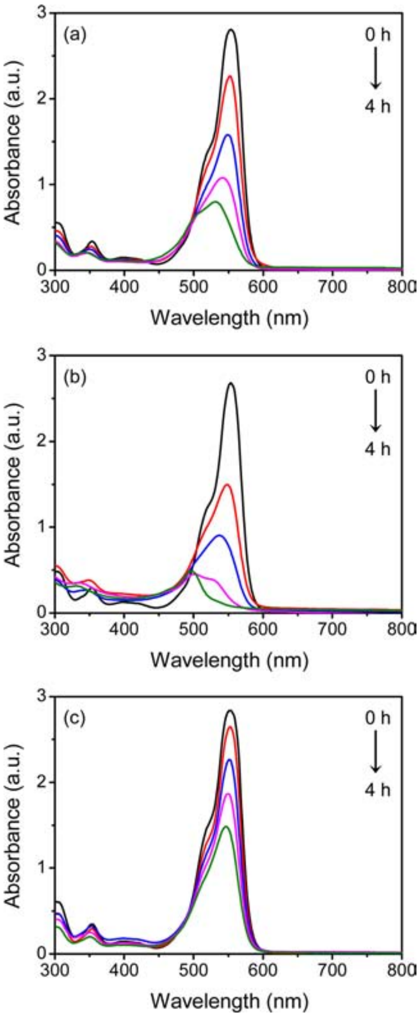

Figure 9. Absorption changes of the RhB aqueous solutions as a function of irradiation time under visible-light (λ > 420 nm) irradiation in the presence of (a) as-prepared $Ag_2Mo_3O_{10}\cdot 2H_2O$ NWs, (b) $Ag@Ag_2Mo_3O_{10}\cdot 2H_2O$ nanocomposite, and (c) N-P25 (after 0 (black), 1 (red), 2 (blue), 3 (purple), and 4 (green) h).

8. EXPERIMENTAL SECTION

Methylamine hydrochloride, $H_3CNH_2\cdot HCl$, $Na_2MoO_4\cdot 2H_2O$, and $AgNO_3$ were purchased from Aldrich. All reagents were used without further purification.

Synthesis of $(CH_3NH_3)_2[Mo_7O_{22}]$. $Na_2MoO_4\cdot 2H_2O$ (2.42 g, 10 mmol) was dissolved in 10 mL of water. After addition of $CH_3NH_2\cdot HCl$ (2.02 g, 30 mmol), the pH was adjusted with 4 M HCl until it reaches 1. The mixture was stirred at room temperature for a few minutes and sealed in a 30 mL Teflon-lined autoclave (120 °C, 6 h, autogenous pressure). The slurry was filtered to isolate a white solid. The powder was washed with H_2O and EtOH and dried in air at room temperature. Yield in Mo: 95%. This new optimized synthesis route differs from the previously reported method employing a higher temperature (200 °C) and a longer reaction time (4 days).[39] FT-IR (cm^{-1}): $CH_3NH_3^+$ cations, 1506 (m), 1460 (w), 1433 (w), 1386 (sh), 1049 (w); ν(Mo=O, Mo−O−Mo), 980 (w), 957 (s), 939 (s), 928 (s), 906 (m), 880 (m), 852 (vs), 746 (m), 702 (s), 652 (s), 569 (s), 536 (m), 472 (w), 459 (sh). $(CH_3NH_3)_2[Mo_7O_{22}]$ has been also well characterized by FT-Raman spectroscopy, which is a very powerful tool to easily identify the nature and topology of the POM blocks in microcrystalline powdered materials.[40,41] Comparison of the Raman spectra of $(CH_3NH_3)_2[Mo_7O_{22}]$ and $(H_3N{-}(CH_2)_6{-}NH_3)_2[Mo_7O_{22}]\cdot H_2O$,[41] i.e., a ${}^2/_\infty[Mo_7O_{22}]^{2-}$ containing hybrid reference, is displayed in Figure S5, Supporting Information, which shows identical Raman signatures of the ${}^2/_\infty[Mo_7O_{22}]^{2-}$ block into both materials.

Synthesis of $Ag_2Mo_3O_{10}\cdot 2H_2O$. $AgNO_3$ (313 mg, 1.84 mmol) was dissolved in 30 mL of 0.1 M HNO_3. After addition of $(CH_3NH_3)_2[Mo_7O_{22}]$ (400 mg, 0.368 mmol), the mixture was stirred at atmospheric pressure at 80 °C for 3 h and filtered to isolate a pale yellow solid (the final pH of the solution was 0.6). The powder was washed with 0.1 M HNO_3, H_2O, and EtOH and dried in air at room temperature. Yield in Mo: 92%. FT-IR (cm^{-1}): H_2O, 1626 (w); ν(Mo=O, Mo−O−Mo), 945 (s), 920 (s), 895 (vs), 864 (m), 730 (m), 650 (vs), 552 (vs), 503 (vs), 438 (m). Raman spectra of $Ag_2Mo_3O_{10}\cdot 2H_2O$ and $(H_2DABCO)[Mo_3O_{10}]\cdot H_2O$ are given in Figure S6, Supporting Information, showing the Raman signature of the ${}^1/_\infty[Mo_3O_{10}]^{2-}$ block similar in the two compounds.

Synthesis of $(H_2DABCO)[Mo_3O_{10}]\cdot H_2O$. White powder of $(H_2DABCO)[Mo_3O_{10}]\cdot H_2O$ has been synthesized according to the reported procedure.[16]

Powder X-ray Diffraction. The pure powder material was examined by X-ray diffraction using a D8 Bruker diffractometer in the Bragg−Brentano geometry, equipped with a front germanium monochromator, a copper anode (CuK-L3 radiation, λ = 1.540598 Å), and a LynxEye PSD detector. To obtain enough information in the high 2θ region and thus accurately locate the oxygen atoms belonging to the water molecules, scanning was done from 10° to 120° with a 0.017° step for a total acquisition time of 6 h.

Scanning Electron Microscopy. Powder morphologies were observed using a scanning electron microscope (SEM). SEM images were taken in a high-magnification microscope JEOL JSM-6400F. For SEM studies, samples were prepared by spreading a small amount of powder on a carbon tape pasted over a copper metal sample holder.

Infrared Spectroscopy. FT-IR spectra were recorded in the 4000−400 cm^{-1} range on a BRUKER Vertex equipped with a computer control using the OPUS software. Near-infrared diffuse reflectance spectra were acquired with a spectral resolution of 4 cm^{-1}, with the praying mantis device (Harrick, DVC).

Raman Spectroscopy. FT-Raman spectra were collected at room temperature under an excitation wavelength of 1064 nm (Nd:YAG laser) using a FT-Raman Bruker RFS 100 spectrophotometer. The nominal power was modulated between 100 and 340 mW to avoid any degradation of the materials. Spectra were recorded at 4 cm^{-1} resolution over the wavenumber range 100−3500 cm^{-1}, with a 100 scan accumulation.

Thermogravimetric Analyses. Differential scanning calorimetry (DSC) and thermogravimetric analysis (TGA) were measured in a flux of dry argon with a heating and cooling rate of 5 °C/min on a SETARAM TG-DSC 111 between 20 and 800 °C.

Brunauer−Emmett−Teller (BET) Analysis. BET method was done in a micrometrics ASAP 2010.

Diffuse Reflectance Spectroscopy. Diffuse reflectivity spectra were collected at room temperature on a finely ground sample with a Cary 5G spectrometer (Varian) equipped with a 60 mm diameter integrating sphere and computer control using the "Scan" software. Diffuse reflectivity was measured from 250 to 1500 nm (i.e., from 5.00 to 0.83 eV) with a 2 nm step using Halon powder (from Varian) as reference (100% reflectance). Reflectivity data were treated by a Kubelka−Munk transformation[42] to obtain the corresponding absorption data and hence better locate the absorption thresholds. Samples were irradiated with a Fisher Bioblock labosi UV lamp (λ_{exc} = 254 nm, P = 6W).

TEM and EELS Microscopy. TEM experiments of the samples were performed on a Hitachi HF 2000 (Field Emission Gun, 100 KV) with a probe diameter of about 7 nm. Irradiation was performed ex situ by directly positioning the TEM sample holder under a UV lamp (254 nm, 6 W) for 4 h to ensure complete irradiation of all the probed material. Moreover, samples before and after UV irradiation were cooled at liquid nitrogen temperature to prevent growth of Ag^0 nanoparticles under electron beam irradiation. EELS spectra were recorded on a modified Gatan 666 parallel spectrometer equipped with a CCD camera and a Digipeels command. The energy resolution was 1.5 eV (given by the zero loss peak full width at half-maximum) with a dispersion of 0.2 eV/pixel. Convergence and collection angles were, respectively, 1.4 and 18.2 mrad. All spectra were dark count and gain corrected.

XPS and Auger Spectroscopy. X-ray photoemission spectra were performed on a Kratos AXIS Ultra spectrometer using a monochromatic Al Kα X-ray source (1486.6 eV). The X-ray source runs at 150 W. The base pressure in the analysis chamber was 10^{-8} Pa, and the analyzed area was 700 × 300 μm^2. The hemispherical analyzer was used in constant analyzer energy (CAE) mode for all spectra. The pass energy was 40 eV for narrow scan and valence band (VB). The energy scale was calibrated using Au $4f_{7/2}$ at 83.97 eV and Cu $2p_{3/2}$ peaks at 932.63 eV measured from sputter-cleaned Au and Cu films.[43] The overall energy resolution, as determined using the Fermi edge of an Ag reference, was 0.47 ± 0.03 at 40 eV pass energy. Samples were ground and pressed into 6 mm diameter pellets, mounted on double-sided carbon tape on an aluminum plate, and quickly transferred from the glovebox to the XPS spectrometer. The charge neutralizer induces polarization of the surface of about +2.2 ± 0.3 V. C 1s and O 1s peaks were also measured in order to check the cleanliness of the samples. The sample contamination contribution was very low, and its impact on the valence band shape change could be neglected. The energy scale was calibrated using C 1s peak position (284.6 eV). The binding energy was referred to the Fermi level (E_F) at BE = 0 eV.

Photocatalytic Experiments. Photocatalytic performance of the as-prepared (yellow pale) and UV-irradiated (dark gray) (i.e., irradiated at 254 nm with a 30 W UV lamp for 6 h) $Ag_2Mo_3O_{10}\cdot 2H_2O$ NWs were evaluated by degradation of Rhodanmine B dye (RhB) under Xe arc lamp irradiation (300 W) with UV cutoff (λ > 420 nm). In a typical experiment, 50 mg samples were dispersed in 100 mL of RhB aqueous solutions (20 mg/L). Before irradiation, suspensions were stirred in the dark for 1 h to establish an adsorption−desorption equilibrium. Then, the above suspension was exposed to light irradiation. A 3 mL solution was taken during the experiments every 1 h and centrifuged to remove the catalysts completely. The solution was analyzed by a UV−vis spectrophotometer (UV-7502pcs, Xinmao, Co. Ltd.). For comparison, N-doped P25 was prepared[44] from P25 placed in a tubular furnace and kept at 773 K for 10 h under NH_3 flow (flow rate of 300 mL/min).

Computational Method. The electronic structure of $Ag_2Mo_3O_{10}\cdot 2H_2O$ was investigated on the basis of spin-polarized density functional theory (DFT) calculations. These employed the projected augmented wave method encoded in the Vienna ab initio simulation package,[45] the generalized gradient approximation (GGA) of Perdew, Burke, and Ernzerhof[46] for the exchange-correlation correction with the plane wave cutoff energy of 550 eV, a set of 2 × 6 × 4 k points, and the threshold 10^{-6} eV for self-consistent-field energy convergence. For optimization of the crystal structure of $Ag_2Mo_3O_{10}\cdot 2H_2O$ as well as its derivatives $Ag_2Mo_3O_{10}\cdot H_2O$ resulting from loss of a H_2O molecule, only the atom positions were optimized on the basis of GGA calculations with force convergence threshold of 0.05 eV/Å. Optimized atom positions of $Ag_2Mo_3O_{10}\cdot 2H_2O$ and $Ag_2Mo_3O_{10}\cdot H_2O$ are given in the Supporting Information.

ASSOCIATED CONTENT

Supporting Information

X-ray crystallographic data of $Ag_2Mo_3O_{10}\cdot 2H_2O$ in CIF format; powder X-ray diffraction data and DSC/TGA measurements of $Ag_2Mo_3O_{10}\cdot 2H_2O$; Mo3d XPS spectra of $Ag_2Mo_3O_{10}\cdot 2H_2O$ and $Ag@Ag_2Mo_3O_{10}\cdot 2H_2O$; PDOS plots for the optimized structure of $Ag_2Mo_3O_{10}\cdot 2H_2O$; near-infrared diffuse reflectance spectra; FT-Raman spectra. This material is available free of charge via the Internet at http://pubs.acs.org.

AUTHOR INFORMATION

Corresponding Author

*Fax: (+33)240-373-995. E-mail: remi.dessapt@cnrs-imn.fr.

Notes

The authors declare no competing financial interest.

ACKNOWLEDGMENTS

The authors are grateful to Pr. Bernard Humbert, Institut des Matériaux Jean Rouxel, France, for fruitful discussions on the IR and Raman characterization of the reported materials.

This work was supported by CNRS and the Ministère de l'Education Nationale, de l'Enseignement Supérieur et de la Recherche.

REFERENCES

(1) (a) Tian, Y.; Tatsuma, T. *J. Am. Chem. Soc.* **2005**, *127*, 7632–7637. (b) Wang, P.; Huang, B.; Dai, Y.; Whangbo, M.-H. *Phys. Chem. Chem. Phys.* **2012**, *14*, 9813–9825.

(2) (a) Primo, A.; Marino, T.; Corma, A.; Molinari, R.; Garcia, H. *J. Am. Chem. Soc.* **2011**, *133*, 6930–6933. (b) Liu, Z.; Hou, W.; Pavaskar, P.; Aykol, M.; Cronin, S. B. *Nano Lett.* **2011**, *11*, 1111–1116.

(3) (a) Chen, X.; Zhu, H.-Y.; Zhao, J.-C.; Zheng, Z.-F.; Gao, X.-P. *Angew. Chem., Int. Ed.* **2008**, *47*, 5353–5356. (b) Hu, C.; Peng, T.; Hu, X.; Nie, Y.; Zhou, X.; Qu, J.; He, H. *J. Am. Chem. Soc.* **2010**, *132*, 857–862.

(4) Wang, P.; Huang, B.; Qin, X.; Zhang, X.; Dai, Y.; Whangbo, M.-H. *Inorg. Chem.* **2009**, *48*, 10697–10702.

(5) Jin, R.; Cao, Y. C.; Mirkin, C. A.; Kelly, K. L.; Scahtzand, G. C.; Zheng, J. G. *Science* **2001**, *294*, 1901–1903.

(6) (a) Acharya, H.; Sung, J.; Sohn, B.-H.; Kim, D. H.; Tamada, K.; Park, C. *Chem. Mater.* **2009**, *21*, 4248–4255. (b) Link, S.; Mohamed, M. B.; El-Sayed, M. A. *J. Phys. Chem. B* **1999**, *103*, 3073–3077.

(7) (a) Wang, P.; Huang, B.; Qin, X.; Zhang, X.; Dai, Y.; Wei, J.; Whangbo, M.-H. *Angew. Chem., Int. Ed.* **2008**, *47*, 7931–7933. (b) Wang, P.; Huang, B.; Zhang, X.; Qin, X.; Jin, H.; Dai, Y.; Wang, Z.; Wei, J.; Zhan, J.; Wang, S.; Wang, J.; Whangbo, M.-H. *Chem.—Eur. J.* **2009**, *15*, 1821–1824.

(8) Wang, P.; Huang, B.; Lou, Z.; Zhang, X.; Qin, X.; Dai, Y.; Zheng, Z.; Wang, X. *Chem.—Eur. J.* **2010**, *16*, 538–544.

(9) Wang, P.; Huang, B.; Zhang, X.; Qin, X.; Dai, Y.; Wang, Z.; Lou, Z. *ChemCatChem.* **2011**, *3*, 360–364.

(10) (a) Xie, Y.; Ding, K.; Liu, Z.; Tao, R.; Sun, Z.; Zhang, H.; An, G. *J. Am. Chem. Soc.* **2009**, *131*, 6648–6649. (b) Zheng, Y.; Zheng, L.; Zhan, Y.; Lin, X.; Zheng, Q.; Wei, K. *Inorg. Chem.* **2007**, *46*, 6980–6986. (c) Paramasivam, I.; Macak, J. M.; Schmuki, P. *Electrochem. Commun.* **2008**, *10*, 71–75. (d) Zheng, Z.; Huang, B.; Qin, X.; Zhang, X.; Dai, Y.; Whangbo, M.-H. *J. Mater. Chem.* **2011**, *21*, 9079–9087.

(11) Hoffmann, M. R.; Martin, S. T.; Choi, W.; Bahnemann, D. W. *Chem. Rev.* **1995**, *95*, 69–96.

(12) (a) Naoi, K.; Ohko, Y.; Tatsuma, T. *J. Am. Chem. Soc.* **2004**, *126*, 3664–3668. (b) Zhang, H.; Wang, G.; Chen, D.; Lv, X.; Li, J. *Chem. Mater.* **2008**, *20*, 6543–6549. (c) Yu, J.; Xiong, J.; Cheng, B.; Liu, S. *Appl. Catal., B* **2005**, *60*, 211–221. (d) Sung-Suh, H. M.; Choi, J. R.; Hah, H. J.; Koo, S. M.; Bae, Y. C. *J. Photochem. Photobiol., A* **2004**, *163*, 37–44. (e) Xin, B.; Jing, L.; Ren, Z.; Wang, B.; Fu, H. *J. Phys. Chem. B* **2005**, *109*, 2805–2809. (f) Stathatos, E.; Lianos, P.; Falaras, P.; Siokou, A. *Langmuir* **2000**, *16*, 2398–2400. (g) Christopher, P.; Ingram, D. B.; Linic, S. *J. Phys. Chem. C* **2010**, *114*, 9173–9177.

(13) (a) Ohtani, B.; Okugawa, Y.; Nishimoto, S.-I.; Kagiya, T. *J. Phys. Chem.* **1987**, *91*, 3550–3555. (b) Sobana, N.; Muruganadham, M.; Swaminathan, M. *J. Mol. Catal. A: Chem.* **2006**, *258*, 124–132. (c) Cozzoli, P. D.; Fanizza, E.; Comparelli, R.; Curri, M. L.; Agostino, A. *J. Phys. Chem. B* **2004**, *108*, 9623–9630.

(14) Feng, M.; Zhang, M.; Song, J.-M.; Li, X.-G.; Yu, S.-H. *ACS Nano* **2011**, *5*, 6726–6735.

(15) H_2DABCO^{2+} ($N_2C_6H_{14}{}^{2+}$) corresponds to the diprotonated 1,4-diazabicyclo[2.2.2]octane cation.

(16) Coué, V.; Dessapt, R.; Bujoli-Doeuff, M.; Evain, M.; Jobic, S. *Inorg. Chem.* **2007**, *46*, 2824–2835.

(17) Rietveld, H. *J. Appl. Crystallogr.* **1969**, *2*, 65–71.

(18) Petricek, V.; Dusek, M.; Palatinus, L. *JANA 2006, a Crystallographic Computing System*; Institute of Physics, Academy of Sciences of the Czech Republic: Prague, Czech Republic, 2000.

(19) Wlodarczyk-Gajda, B.; Rafalska-Lasocha, A.; Lasocha, W. *Powder Diffr.* **2007**, *22*, 241–245.

(20) Cheary, R. W.; Coelho, A. A. *J. Appl. Crystallogr.* **1992**, *25*, 109–121.

(21) Cheary, R. W.; Coelho, A. A. *J. Appl. Crystallogr.* **1998**, *31*, 862–868.

(22) Dollase, W. A. *J. Appl. Crystallogr.* **1986**, *19*, 267–272.

(23) Brown, I. D.; Altermatt, D. *Acta Crystallogr., Sect. B: Struct. Sci* **1985**, *41*, 244–247.

(24) (a) Cheng, L.; Shao, Q.; Shao, M.; Wei, X.; Wu, Z. *J. Phys. Chem. C* **2009**, *113*, 1764–1768. (b) Hashim, M.; Hu, C.; Chen, Y.; Zhang, C.; Xi, Y.; Xu, J. *Phys. Status Solidi A* **2011**, *208*, 1937–1941. (c) Cui, X.; Yu, S.-H.; Li, L.; Biao, L.; Li, H.; Mo, M.; Liu, X.-M. *Chem.—Eur. J.* **2004**, *10*, 218–223. (d) Bao, Z.; Zhang, L.; Wu, Y. *Front. Optoelectron. China* **2011**, *4*, 166–170.

(25) Liu, W.; Ji, M.; Chen, S. *J. Hazard. Mater.* **2011**, *186*, 2001–2008.

(26) Coué, V.; Dessapt, R.; Bujoli-Doeuff, M.; Evain, M.; Jobic, S. *J. Solid. State Chem.* **2008**, *181*, 1116–1122.

(27) Kim, D. W.; Cho, I.-S.; Lee, S.; Bae, S.-T.; Shin, S. S.; Han, G. S.; Jung, H. S.; Hong, K. S. *J. Am. Ceram. Soc.* **2010**, *93*, 3867–3872.

(28) (a) Yamase, T. *Chem. Rev.* **1998**, *98*, 307–325. (b) Dessapt, R.; Collet, M.; Coué, V.; Bujoli-Doeuff, M.; Jobic, S.; Lee, C.; Whangbo, M.-H. *Inorg. Chem.* **2009**, *48*, 574–580. (c) Dessapt, R.; Gabard, M.; Bujoli-Doeuff, M.; Deniard, P.; Jobic, S. *Inorg. Chem.* **2011**, *50*, 8790–8796.

(29) (a) Aguirre, M. E.; Rodriguez, H. B.; San Román, E.; Feldhoff, A.; Grela, M. A. *J. Phys. Chem. C* **2011**, *115*, 24967–24974. (b) Epifani, M.; Giannini, C.; Tapfer, L.; Vasanelli, L. *J. Am. Ceram. Soc.* **2000**, *83*, 2385–93. (c) Awazu, K.; Fujimaki, M.; Rockstuhl, C.; Tominaga, J.; Murakami, H.; Ohki, Y.; Yoshida, N.; Watanabe, T. *J. Am. Chem. Soc.* **2008**, *130*, 1676–1680.

(30) Ahn, C. C.; Krivanek, O. L. *EELS Atlas*; Gatan: Warrendale, 1983.

(31) Wertheim, G. K.; Schneemeyer, L. F.; Buchanan, D. N. E. *Phys. Rev. B* **1985**, *32*, 3568–3572.

(32) (a) Gaarenström, S. W.; Winograd, N. *J. Chem. Phys.* **1977**, *67*, 3500–3506. (b) Tjeng, L. H.; Meinders, M. B. J.; Van Elp, J.; Ghijsen, J.; Sawatzky, G. A. *Phys. Rev. B* **1990**, *41*, 3190–3199. (c) Rivers, S. B.; Bernhardt, G.; Wright, M. W.; Frankel, D. J.; Steeves, M. M.; Lad, R. J. *Thin Solid Films* **2007**, *515*, 8684–8688. (d) Bielmann, M.; Schwaller, P.; Ruffieux, P.; Gröning, O.; Schlapbach, L.; Gröning, P. *Phys Rev. B* **2002**, *65*, 235431.

(33) Kaushik, V. K. *J. Electron Spectrosc. Relat. Phenom.* **1991**, *56*, 273–277.

(34) Hüfner, S.; Wertheim, G. K.; Smith, N. V.; Traum, M. M. *Solid State Commun.* **1972**, *11*, 323–326.

(35) He, T.; Yao, J. *J. Photochem. Photobiol., C* **2003**, *4*, 125–143.

(36) (a) Lehmani, A.; Turq, P.; Simonin, J.-P. *J. Electrochem. Soc.* **1996**, *143*, 1860–1866. (b) Farmer, J. C.; Wang, F. T.; Hawley-Fedder, R. A.; Lewis, P., R.; Summers, L., J.; Foiles, L. *J. Electrochem.*

Soc. **1992**, *139*, 654−662. (c) Grochala, W.; Hoffman, R. *Angew. Chem., Int. Ed. Engl.* **2001**, *40*, 2743−2781.

(37) Fu, H. B.; Pan, C. S.; Yao, W. Q.; Zhu, Y. F. *J. Phys. Chem. B* **2005**, *109*, 22432−22439.

(38) Yu, X.; Yu, J. G.; Cheng, B.; Huang, B. *Chem.—Eur. J.* **2009**, *15*, 6731−6739.

(39) Zavalij, P. Y.; Whittingham, M. S. *Acta Crystallogr.* **1997**, *C53*, 1374−1376.

(40) Dessapt, R.; Kervern, D.; Bujoli-Doeuff, M.; Deniard, P.; Evain, M.; Jobic, S. *Inorg. Chem.* **2010**, *49*, 11309−11316.

(41) Bujoli-Doeuff, M.; Dessapt, R.; Deniard, P.; Jobic, S. *Inorg. Chem.* **2012**, *51*, 142−149.

(42) Kubelka, P.; Munk, F. *Z. Tech. Phys.* **1931**, *12*, 593−601.

(43) Seah, M. P.; Gilmore, I. S.; Beamson, G. *Surf. Interface Anal.* **1998**, *26*, 642−649.

(44) Maeda, K.; Shimodaira, Y.; Lee, B.; Teramura, K.; Lu, D.; Kobayashi, H.; Domen, K. *J. Phys. Chem. C* **2007**, *111*, 18264−18270.

(45) (a) Kresse, G.; Hafner, J. *Phys. Rev. B* **1993**, *47*, 558−561. (b) Kresse, G.; Furthmüller, J. *Comput. Mater. Sci.* **1996**, *6*, 15−50. (c) Kresse, G.; Furthmüller, J. *Phys. Rev. B* **1996**, *54*, 11169−11186.

(46) Perdew, J. P.; Burke, K.; Ernzerhof, M. *Phys. Rev. Lett.* **1996**, *77*, 3865−3868.